Experiments and numerical simulations of single particle foreign object damage-like impacts of thermal barrier coatings☆

M.W. Crowell [a,*], T.A. Schaedler [b], B.H. Hazel [d], D.G. Konitzer [d], R.M. McMeeking [e,c,f], A.G. Evans [c,e]

[a] Los Alamos National Laboratory, Los Alamos, NM 87545, USA
[b] HRL Laboratories, 3011 Malibu Canyon Rd., Malibu, CA 90265, USA
[c] Materials Department, University of California, Santa Barbara, CA 93106-5050, USA
[d] General Electric Aviation, One Neumann Way, Cincinnati, OH 45215, USA
[e] Department of Mechanical Engineering, University of California, Santa Barbara, CA 93106-5070, USA
[f] School of Engineering, University of Aberdeen, King's College, Aberdeen AB24 3UE, Scotland

ARTICLE INFO

ABSTRACT

The thermal barrier coatings (TBCs) used on the hot section components of many aero-turbines face a variety of compromising conditions while in service. One condition of particular concern on high-pressure turbine (HPT) blades is foreign object damage (FOD) wherein hard foreign particles, often found in the gas path of operating aero-turbines, are struck by the leading edge of the HPT blades. Even single impacts of this kind can cause complete spallation of the local TBC, removing thermal protection on one of the hottest component surfaces in the entire engine. We present here the first experimental FOD study we know of where the impacting particle size, geometry, and velocity, as well as TBC temperature, are well known at each impact site. We then quantitatively compare the experimental impact crater profiles with numerical simulations of equivalent impact scenarios, finding excellent agreement and thereby validating the numerical modeling techniques and parameters. Finally, we present a numerical parameter study of particle and TBC material properties using the validated model.

© 2012 Elsevier Ltd. All rights reserved.

1. Introduction

Thermal barrier coatings (TBCs) are widely used in the hot section of aviation gas turbine engines to provide thermal insulation for the nickel-based superalloy components found therein. Standard TBCs consist of 7 wt.% yttria stabilized zirconia (7YSZ) applied over an oxidation resistant metallic bond coat with a thermally grown oxide (TGO) forming at the interface. TBCs on high-pressure turbine blades are generally deposited by electron beam physical vapor deposition (EB-PVD), resulting in a columnar microstructure with excellent in-plane strain tolerance. TBCs are very effective at further reducing operating temperatures of the underlying actively cooled superalloy components, but face many scenarios during service that can lead to degradation and failure, limiting their benefits [1]. One such scenario is particle impact or "foreign object damage" (FOD). Particles ingested into or liberated within gas turbine engines can collide with coated components and cause damage to TBCs (Fig. 1). Rotating blades are most susceptible

to impact damage because their high rotational speeds result in large particle/TBC impact velocities, despite the relatively low velocities associated with the particles themselves [2]. Prior experiments and modeling [3–6] have shown that elastic waves are initiated in the TBC upon impact of a particle. The elastic waves are reflected at the TBC/TGO interface and produce tensile stresses that can be large enough to cause spallation of the TBC. As the particle penetrates into the TBC, plastic deformation occurs, leading to densification and column bending. The deformation is often accompanied by shear bands, which extend diagonally downward and, in some cases, induce delamination along the interface with the TGO [3,5].

The conditions leading to FOD in a jet engine are complex and encompass a range of impact angles, impact speeds, particle sizes, particle compositions, and material temperatures [2]. Therefore, a dynamic finite element model has been developed to help the understanding and prediction of foreign object damage [4,5]. In this article a laboratory experimental setup capable of producing highly controlled individual FOD-like impacts is described. The results from this experimental setup are used to validate the parameters and modeling approach used previously [4,5], rendering it a more effective tool for both understanding and predicting FOD. The article is organized as follows: Laboratory FOD testing is described

Fig. 1. Image of the leading edge of an engine-run high-pressure turbine blade showing severe foreign object damage. Note the large gray region which indicates bond coat exposed by complete removal of the TBC.

in Section 2 and the numerical modeling in Section 3. Section 4 contains analysis which enables the quantitative comparison of experimental and modeling results, and guides the selection of relevant modeling parameters. Sections 5 and 6 then present the experimental and simulation results and comparisons enabled by the analysis in Section 4. Finally, Section 7 contains a discussion of the findings and conclusions.

2. Experimental setup

Fig. 2 shows a schematic of the ballistic impact test utilized. It is used to mimic particle impact by shooting projectiles at samples with a gas gun, consisting of a barrel with a 4.5 mm (0.177″) bore connected to a pressurized gas cylinder. The speed of the projectile can be set reliably by adjusting the gas pressure and is recorded with a ballistic chronograph with two photoelectric screens (Oehler Research Inc., Austin, TX). Balls 4.4 mm in diameter (dictated by the barrel bore), made of 2024 aluminum alloy, were selected as projectiles. Particles of this great size are not likely to occur in the engine, but the large diameter facilitates the experiments and their analysis. Furthermore, trials with projectiles of a variety of materials showed that post-impact TBC microstructures similar to those observed in field service were achieved best with 4.4 mm aluminum particles. Aluminum 2024 exhibits a yield strength at room temperature of approximately 200 MPa [7], which is representative of impacting oxide particles at gas turbine temperatures [8, 9]. Room temperature aluminum projectiles therefore emulate

such impacting oxide particles heated in the gas stream of the engine.

Conventional TBCs were applied by EB-PVD to 1″ diameter buttons of René® N5 nickel-based superalloy coated with a diffusion platinum modified aluminide bond coating. The TBC coated buttons were tack-welded to sample holders of Hastelloy® X and clamped into the test setup. An effort was made to assure rigid mounting of the TBC sample, but some vibration after impact could not be avoided. The specimens were heated by induction, while the temperature was measured with a thermocouple on the back of the sample holder. After ramp up to a temperature of 1093 °C (2000 °F) in 5 min, each sample was allowed to sit at this temperature for 2 min. It was then impacted by a particle shot between the coils of the induction heater and subsequently cooled down in air. Finally, the width and depth of each impact site on each button was measured via light microscopy (Zeiss Axioskop) and optical profilometry (Wyko Optical Profiler) respectively. Due to difficulties in obtaining optical profilometry measurements of the highly scattering TBC surface, replicas of the impact impressions were taken with ReproRubber® (Flexbar Corp., Long Island, NY) and measured subsequently. Examples of these measurements are found in Fig. 3.

3. Simulation setup

In order to characterize the experimental conditions in a numerical simulation, the large diameter of the impacting particle (4.4 mm) relative to the small column diameter of the TBC ($\sim 8\ \mu m$) necessitates a large, expensive computation. The axial symmetry of the impacting particle might suggest the use of a 2D axi-symmetric simulation, but this would fundamentally misrepresent the microstructure of the TBC. One of the major deformation modes present in TBCs subject to FOD is kink bands, which have been shown to be planar in nature *even when induced by a spherical particle* and thus cannot be reproduced in axi-symmetric simulations [5,6,9]. We have therefore chosen 2D plane-strain simulations where the TBC is modeled as an array of dense columns fully connected by porous intercolumnar zones, and resting on an elastic (superalloy) substrate. This setup can capture the typical TBC FOD deformation modes such as kink bands that are critical to the study [4–6]. The choice of 2D plane-strain does misrepresent the impacting particle as a cylinder instead of a sphere, but that difference can be corrected for with the analysis we present in Section 4, allowing quantitative comparison of simulation and experimental results. Because the experimental work involves only normal impacts, we make use of the plane of symmetry at the center of the impacting particle, normal to the TBC surface, to further reduce the simulation size. Finally, we do not model the bond coat or TGO. This simplification is assumed to affect the results minimally, due to the similarity of the mechanical properties of bond coat and superalloy and the negligible thickness of the TGO [4,5]. The resulting simulation geometry is shown in Fig. 4.

3.1. Constitutive laws

The impacting particle is modeled as isotropic with strain hardening of the form:

$$\sigma_y^{par} = \sigma_o^{par} + \left(\sigma_y^{*\,par} - \sigma_o^{par} \right) \left[1 - e^{-\left(\frac{\varepsilon_p}{\lambda} \right)} \right], \tag{1}$$

where σ_y^{par} is the particle yield strength, $\sigma_y^{*\,par}$ is the phonon drag limited yield strength [10], σ_o^{par} is the initial particle yield strength, ε_p is the equivalent plastic strain, and $\lambda = \varepsilon_c^{par}/\sqrt{\ln 2}$. The parameter ε_c^{par} is the critical plastic strain at which
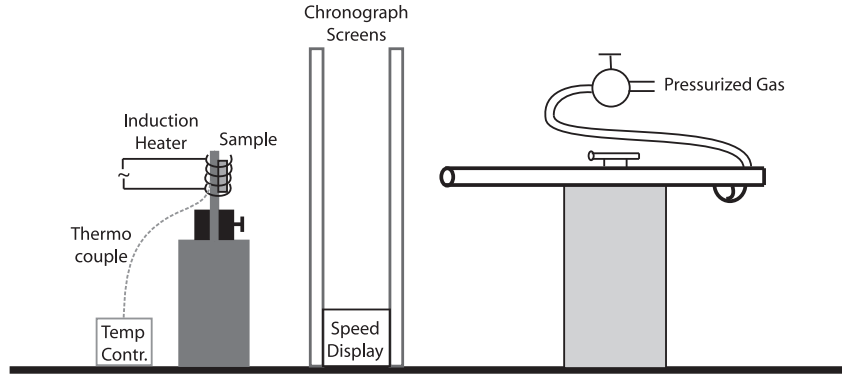
Fig. 2. Schematic of the ballistic impact testing rig, including gas gun, chronograph, sample holder, and induction heater/temperature control.

$\sigma_y^{par} = (\sigma_y^{*\,par} + \sigma_o^{par})/2$. Furthermore, σ_o^{par} is set as a fraction, q_o^{par}, of $\sigma_y^{*\,par}$ such that $q_o^{par} = \sigma_o^{par}/\sigma_y^{*\,par}$. All values are with reference to a uniaxial stress configuration. This strain hardening relation in Eq. (1), along with the phonon drag limited yield strength, is used in lieu of the more typical power law due to the extremely high strain rates ($>10^4\,\mathrm{s}^{-1}$) encountered in these simulations.

The dense TBC columns are modeled using the Gurson constitutive law, which allows for isolated intra-columnar porosity (Fig. 5b) [11]. This law has the yield condition[12,13]:

$$\varphi = \left(\frac{q}{\sigma_y}\right)^2 + 2q_1 f \cosh\left(\frac{3q_2 p}{2\sigma_y}\right) - \left(1 + q_3 f^2\right) = 0, \qquad (2)$$

where σ_y is the uniaxial yield strength, $q = \sqrt{(3/2)s_{ij}s_{ij}}$ is the tensile equivalent stress, $s_{ij} = p\delta_{ij} + \sigma_{ij}$ is the deviatoric part of the macroscopic Cauchy stress tensor, p is the hydrostatic pressure, and f is the volume fraction of voids (initially, $f = 0.1$). Setting parameters $q_1 = q_2 = q_3 = 1$ is the simplest choice found to reproduce the kink-bands observed in quasi-static experiments and field returned engine hardware [4]. This renders the yield condition:

$$\left(\frac{q}{\sigma_y^{col}}\right)^2 + 2f \cosh\left(\frac{3p}{2\sigma_y^{col}}\right) - \left(1 + f^2\right) = 0, \qquad (3)$$

Note we have replaced σ_y with σ_y^{col} to indicate specifically the dense columnar yield strength. No strain hardening is assumed for the dense columns, but again, due to the extremely high strain rates, we expect the yield strength to be dominated by phonon drag: $\sigma_y^{col} \approx \sigma_y^{*\,col}$.

The highly porous intercolumnar zones of the TBC are treated as a low-density crushable medium (Fig. 5c) [5] with isotropic hardening, having the yield surface [14]:

$$\sqrt{q^2 + \alpha^2 p^2} - \alpha p_c = 0, \qquad (4)$$

where p_c is the yield strength in hydrostatic compression, and $\alpha = 3k/\sqrt{9 - k^2}$ where k is the ratio of tensile to compressive hydrostatic yield strengths. We take $k = 1$ [5] which yields $\alpha = 3\sqrt{2}/4$. The parameter p_c is related to the intercolumnar uniaxial yield strength, σ_y^{ic}, by $p_c = \sigma_y^{ic}\sqrt{1 + (\alpha/3)^2}$. We have chosen a foam-like hardening behavior for σ_y^{ic} with an initial yield plateau, followed by a rapid rise once densification commences at a critical nominal compressive strain of $\varepsilon_c = 0.2$. The ultimate yield strength is limited by that for the dense columns, while the initial (plateau) yield strength, σ_o^{ic}, is set as a fraction, q_o^{ic}, of the ultimate yield strength($q_o^{ic} = \sigma_o^{ic}/\sigma_y^{col}$). This behavior is given by:

$$\sigma_y^{ic} = \sigma_o^{ic} + \left(\sigma_y^{col} - \sigma_o^{ic}\right)\left[1 - e^{-\left(\frac{\varepsilon_p}{\lambda}\right)^n}\right], \qquad (5)$$

where the superscripts ic and col denote intercolumnar and dense columnar values, respectively, ε_p is the nominal compressive plastic strain so that the maximum possible value of ε_p is 1, and n is the parameter controlling the slope of the transistion from $\sigma_y^{ic} = \sigma_o^{ic}$ to $\sigma_y^{ic} = \sigma_y^{col}$. n must be greater than zero with higher values corresponding to steeper slopes. Finally, $\lambda = \varepsilon_c/(\ln 2)^{1/n}$ and we have taken $\varepsilon_c = 0.2$. In this manner, the foam-like hardening is completely specified by choice of initial yield strength ratio, q_o^{ic}, the
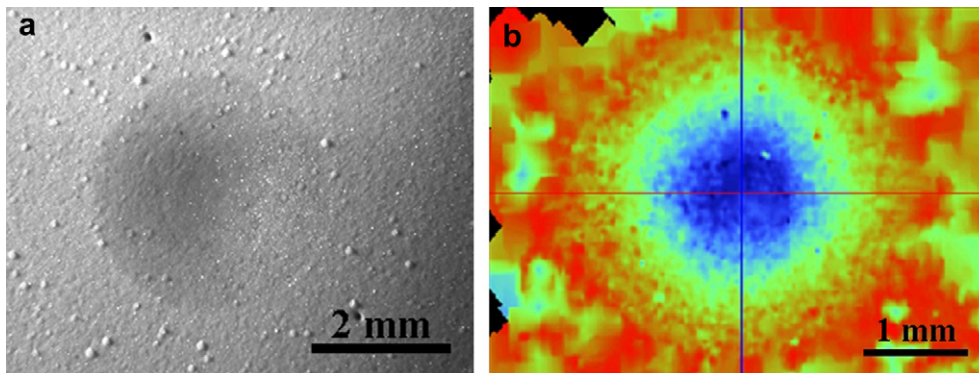

Fig. 3. Examples of impact site measurements: (a) plan view light micrograph, and (b) optical profilometry result.
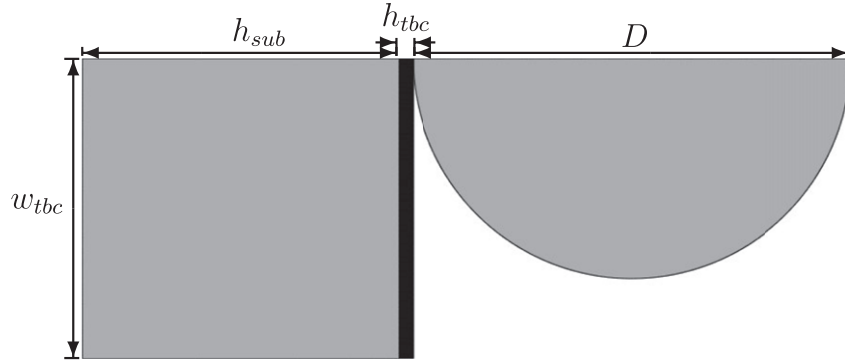
Fig. 4. Schematic of numerical model: symmetry boundary condition at top for all elements and rigid boundary condition at left along substrate base. $D = 4.4$ mm, $w_{tbc} = 3.0$ mm, $h_{tbc} = 145$ µm, and $h_{sub} = 3.175$ mm.

dense column yield strength, σ_y^{col}, and the transition slope parameter, n.

Both the Gurson and the crushable medium models are available as built in materials within the commercial finite element code ABAQUS/EXPLICIT.

3.2. Geometries and boundary conditions

Based on cross-sectional micrographs of the experimental specimens (Fig. 6), we have chosen for our simulations a TBC thickness of $h_{tbc} = 145$ µm, and an overall TBC column width of $b + d = 8$ µm, where b is the dense column width and d is the porous intercolumnar width. We have estimated the ratio of dense to porous column widths as $b/d \approx 4$. The elastic substrate is modeled with a thickness of $h_{sub} = 3.175$ mm (0.125 in), representative of the superalloy button thickness in the experiments. For the impacting particle, a radius of $r = 2.2$ mm is used, consistent with 4.4 mm diameter particles used in the experiments.

The overall half-width of the TBC and substrate is $w_{tbc} = 3.0$ mm. As depicted in Fig. 4, the upper horizontal boundary of the simulation is a plane of symmetry where no vertical (x-axis) displacements are allowed, and the base (left side) of the elastic substrate is rigidly supported. All other boundaries are free.

3.3. Material properties

The dense inner-column regions of the TBC are modeled as having a density of 5900 kg m^{-3}, 10% initial porosity ($f = 0.1$), a Young's modulus when fully dense of 200 GPa, and a Poisson's ratio of 0.25 [5,6,15]. After considering theoretical phonon/electron drag limits on yield strength (Section 4.3) and preliminary simulation results, we set the nominal yield strength to 1300 MPa. Taking the "feathery" outer-column regions of the TBC as the intercolumnar zones (Fig. 5a), we estimate a relative mass density for these zones of $\sim 1/3$. This indicates a density of 2000 kg m^{-3} for use in the crushable medium representation (Fig. 5c). A Young's modulus of 5 GPa is assumed, based on in-plane modulus measurements made by Eberl et al. [16]. The initial yield strength ratio is taken as $q_o^{ic} = 0.5$ and the transition slope parameter as $n = 3$.

For the isotropic elastic substrate we use a density of 8900 kg m^{-3}, a Young's modulus of 200 GPa, and a Poisson's ratio of 0.33, representative of a Ni-based superalloy [4]. The impacting particle is modeled as 2024 aluminum alloy with a density[1] Calculated of 2870 kg m^{-3}, a Young's modulus of 72 GPa, and a Poisson's ratio of 0.33 [7]. The nominal phonon drag limited yield strength of 2024 aluminum, based on theoretical considerations and in light of preliminary simulation results, is taken as 825 MPa. The initial yield strength ratio is taken as $q_o^{par} = 0.75$ and the critical plastic strain as $\varepsilon_c^{par} = 0.02$.

3.4. Parameter variation

The material densities and elastic properties, the TBC and substrate thickness, and the particle diameter are well known, whereas the remaining geometries and material properties (collectively "parameters" hereafter) are not. Therefore, in this study we have both sought out nominal values of the unknown parameters which provide good agreement between the experimental and simulation results, and performed individual variations of each parameter to assess their relative effects on the simulation results. The nominal and varied values of all the parameters are provided in Table 2. Note that for each combination of parameter values the simulations are performed at all impacts speeds (17 parameter combinations × 4 impact speeds = 68 distinct simulations).

4. Analysis to enable interpretation

To facilitate the quantitative comparison of experimental and simulation results, we turn to accepted outcomes of dynamic contact mechanics from Johnson [17]. We will show that two characteristic quantities of the particle/TBC impacts can be compared directly between the simulation and experimental results. These are the mean dynamic contact pressure, p_d, and the TBC deformation relative to the full system (TBC and particle) deformation, V_{tbc}/V_{app}, or simply relative TBC deformation. Furthermore, these quantities can be calculated from readily observable impact crater geometries which cannot themselves be directly compared between the experiments and the simulations.

4.1. Plastic impact of particle and TBC/substrate

We begin with the mean dynamic contact pressure. For a normal impact between two bodies, we can equate the initial kinetic energy of the system to the work done during the impact up to the point of maximum interpenetration:

$$\frac{1}{2}mv^2 = W = \int_0^{\varepsilon^*} P \mathrm{d}\varepsilon. \tag{6}$$

In this expression, m is the relative mass of the system, given by:

$$\frac{1}{m} = \frac{1}{m_1} + \frac{1}{m_2}, \tag{7}$$

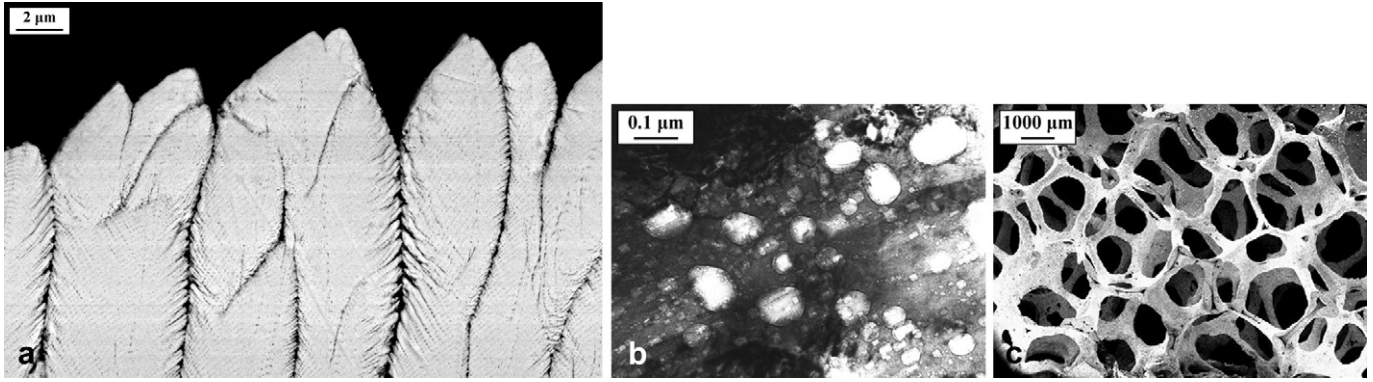[1] Calculated from measured mass and diameters of particles used in experimental work.

Fig. 5. (a) Typical EB-PVD (7YSZ) feathery columnar microstructure. (b) High-resolution transmission electron micrograph of column core indicating residual porosity. (c) An example of a metallic foam used to model the mechanical properties of the feathery intercolumnar zones.

where m_1 and m_2 are the masses of each of the two impacting bodies, v is the relative velocity, P is the contact force, and ε is the interpenetration of the two bodies with ε^* denoting the maximum interpenetration. The contact force, P is given by:

$$P = p_d A, \tag{8}$$

where p_d is the mean dynamic contact pressure and A is the projection of the contact area onto a plane perpendicular to the direction of interpenetration. In the case of a fully plastic impact at moderate speeds ($v \lesssim 500 \text{ m s}^{-1}$), p_d is approximately constant throughout the impact, and equal to the effective hardness of the softer of the two impacting bodies: the particle in this case. So we rewrite Eq. (6) and note that the integral is the apparent volume displaced during the impact, V_{app}, or the total system deformation:

$$\frac{1}{2}mv^2 = p_d \int_0^{\varepsilon^*} A \mathrm{d}\varepsilon = p_d V_{\text{app}}. \tag{9}$$

In both experiment and simulation, the two body impacting system consists of the particle projectile and the TBC coated substrate target. In both cases the TBC coated substrate is so massive relative to the impacting particle as to render the relative mass of the system, m, calculated from Eq. (7), effectively equal to the mass of the particle only:
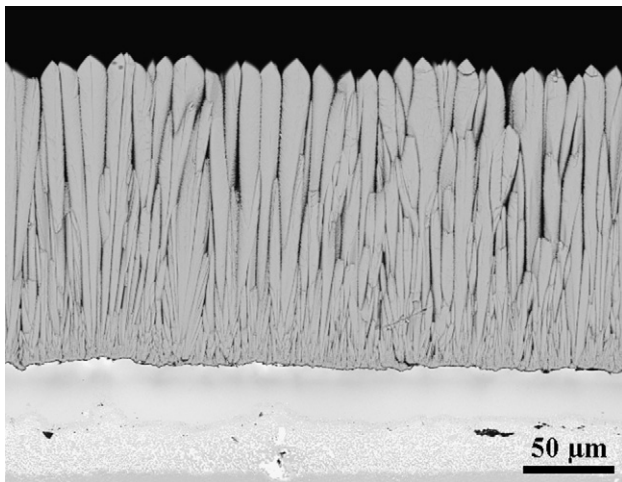
$$m^{\text{exp}} = \frac{4}{3}\pi r^3 \rho \quad m^{\text{sim}} = \pi r^2 t \rho. \tag{10}$$

The exp and sim superscripts refer to experimental and simulation quantities, respectively, ρ is the particle density of 2870 kg m^{-3}, r is the particle radius of 2.2 mm, and t is the thickness of the simulated particle's cylindrical section.

Observation of both experimental and simulation results reveals that the interpenetration, ε, is well characterized by the contact half-width, a, as depicted in Fig. 7. That is, neither the particle nor the TBC/substrate are observed to deform significantly outside of the contact area. Thus we may write ε and its differential, $\mathrm{d}\varepsilon$, as:

$$\varepsilon = r\left[1 - \sqrt{1 - \left(\frac{a}{r}\right)^2}\right], \quad \mathrm{d}\varepsilon = \frac{a}{\sqrt{r^2 - a^2}}\,\mathrm{d}a. \tag{11}$$

Also, the normal projected contact area, A, can be written as:

$$A^{\text{exp}} = \pi a^2 \quad A^{\text{sim}} = 2at. \tag{12}$$

Eqs. (11) and (12) allow the computation of the integrals which define the apparent displaced volumes for the experiments and the simulations:

$$\begin{aligned} V_{\text{app}}^{\text{exp}} &= \int_0^{\varepsilon^*} A^{\text{exp}} \mathrm{d}\varepsilon = \int_0^{a^*} \frac{\pi a^3}{\sqrt{r^2 - a^2}}\,\mathrm{d}a \\ &= \frac{\pi}{3}\left[2r^3 - \sqrt{r^2 - a^{*2}}\left(2r^2 + a^{*2}\right)\right] \end{aligned} \tag{13}$$

Fig. 6. Cross-sectional scanning electron micrograph of a representative as deposited TBC microstructure from the experimental study.
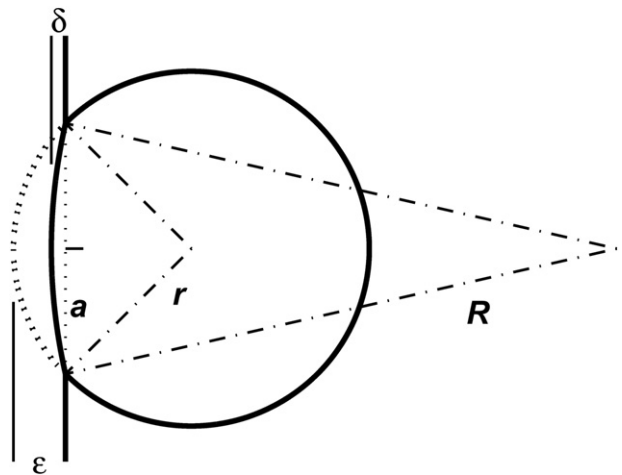

Fig. 7. Schematic of impact geometry.

$$V_{app}^{sim} = \int_0^{\varepsilon^*} A^{sim} d\varepsilon = t \int_0^{a^*} \frac{2a^2}{\sqrt{r^2 - a^2}} da$$
$$= t \left[r^2 \arcsin\left(\frac{a^*}{r}\right) - a^* \sqrt{r^2 - a^{*2}} \right], \qquad (14)$$

where a^* is the contact half-width at maximum interpenetration.

Now we may substitute Eqs. (10), (13), and (14) into Eq. (9) and solve for p_d^{exp} and p_d^{sim}:

$$p_d^{exp} = \frac{\rho v^2}{1 - \sqrt{1 - \left(\frac{a^*}{r}\right)^2 \left[2 + \left(\frac{a^*}{r}\right)^2\right]}} \qquad (15)$$

$$p_d^{sim} = \frac{\pi \rho v^2}{\arcsin\left(\frac{a^*}{r}\right) - \frac{a^*}{r}\sqrt{1 - \left(\frac{a^*}{r}\right)^2}}, \qquad (16)$$

in terms of the known quantities ρ, v, and r, and the readily measurable quantity a^*. Experimental and theoretical results indicate, all else being equal, that the mean contact pressure in the case of plane strain will be ~80 to 90% of that observed in the case of axial symmetry [18]. Even though the experiments are not axisymmetric due to the TBC, the mean contact pressure is dominated by the axi-symmetric particle, thus we expect for a well executed simulation the dynamic pressure will be ~85% of that in the experiments.

4.2. TBC contribution to impact

We now consider the relative TBC deformation. The TBC component of the total deformation may be calculated by substituting the TBC crater depth, δ, for the total interpenetration, ε, in the apparent volume integral:

$$V_{tbc} = \int_0^{\delta^*} A d\delta \qquad (17)$$

Observation of both experimental and simulated TBC residual contact profiles reveals a relatively constant curvature. That is, they are well approximated geometrically by the indent of a rigid sphere or cylinder with radius $R \gg a$, as depicted in Fig. 7. Then, using the fact that $\delta \ll a$, we can approximate R and then $d\delta$ as:

$$R \approx \frac{a^2}{2\delta}, \quad d\delta \approx \frac{a}{R} da. \qquad (18)$$

Substituting Eqs. (12) and (17) into Eq. (16) and computing the integrals we can write the TBC deformation for both the experiments and the simulations:

$$V_{tbc}^{exp} = \frac{\pi}{2} \delta^* a^{*2}, \quad V_{tbc}^{sim} = t \left(\frac{4}{3} \delta^* a^*\right). \qquad (19)$$

Table 1
Material densities and elastic property values.

	E (GPa)	ν	ρ (kg m^{-3})
Impacting particle	72	0.33	2870
TBC columns	200	0.25	5900
TBC intercolumns	5	0.33	2000
Substrate	200	0.33	8900

Table 2
Simulation parameters: nominal values in bold.

TBC columns					Impacting particle			
$b+d$ (μm)	b/d	q_0^{ic}	n	σ_y^{col} (MPa)	q_0^{par}	ε_c	$\sigma_y^{* par}$ (MPa)	v (m s^{-1})
5	3	0.2	2	1150	0.5	0.01	750	50
8	**4**	**0.5**	**3**	**1300**	**0.75**	**0.02**	**825**	**100**
11	6	0.8	7	1450	1.0	0.03	900	**150**
								200

As previously, starred ($*$) variables indicate the values at maximum interpenetration. While we would not expect the experimental and simulation TBC deformations to be directly comparable, we do expect the relative TBC deformations, V_{tbc}/V_{app}, which Eqs. (13), (14), and (19) allow us to calculate, to be comparable.

4.3. Phonon/electron drag limited plasticity

At shear strain rates of ~10^2 s^{-1} or greater we can expect that dislocation velocities will be limited by phonon and/or electron interactions. In such cases, the strain rate is expected to be directly proportional to the stress [10]: $\dot{\gamma} = C(\sigma_s/\mu)$, where $\dot{\gamma}$ is the shear strain rate, C is a constant approximately equal to 5×10^6 s^{-1} [10,19,20], σ_s is the shear stress, and μ is the shear modulus. Restating in terms of axial stress and strain for yield strength as a function of strain rate gives:

$$\sigma_y = \frac{3E}{2(1+\nu)} \frac{\dot{\varepsilon}}{C}, \qquad (20)$$

where σ_y is the axial yield strength, E is the Young's modulus, ν is the Poisson's ratio, and $\dot{\varepsilon}$ is the axial strain rate.

Substituting in the values of E and ν taken in this study for the aluminum particles and the dense 7YSZ TBC columns (Table 1) yields the σ_y versus $\dot{\varepsilon}$ relationships plotted in Fig. 8. These plots also include the theoretical maximum or "ideal" shear strengths given by $\sigma_s \approx 0.1\mu$ [10] or $\sigma_y \approx 0.1\sqrt{3}E/[2(1+\nu)]$ in axial stress/strain. Preliminary simulation results indicated axial strain rates of 10^4–10^6 s^{-1} in both the TBC columns and the impacting particle. Given these strain rates, consulting Fig. 8 indicates we might reasonably expect phonon drag limited dense TBC columnar yield strengths, $\sigma_y^{* col}$, of 0.48–13.9 GPa, and drag limited particle yield strengths, $\sigma_y^{* par}$, of 0.16–4.7 GPa. Recall that although $\sigma_y^{* col}$ does
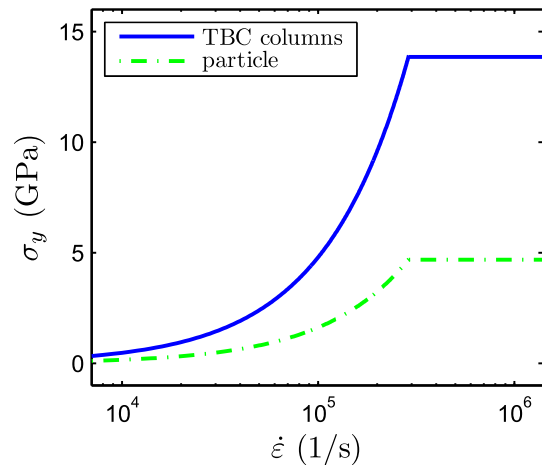

Fig. 8. Theoretical drag limited yield strength versus strain rate for the TBC columns and impacting particle. Note the plateau at high strain rates which corresponds to the maximum or "ideal" yield strength.
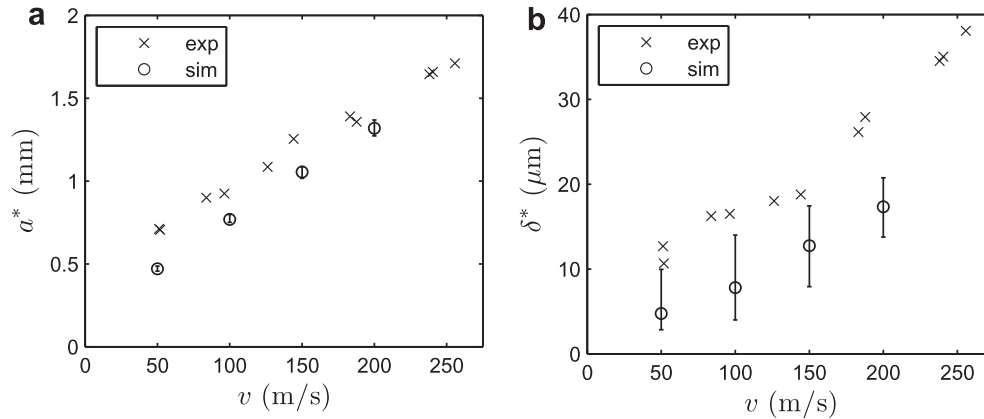
Fig. 9. Experimental and simulation results for (a) contact half-width, a^*, and (b) residual TBC indentation depth, δ^*, versus impact speed, v.

not appear directly in the yield condition for the TBC columns (Eq. (3)), we are assuming $\sigma_y^{col} \approx \sigma_y^{*\,col}$ due to the high strain rates. Due to the paucity of experimental data at such high strain rates, we must rely on these broad theoretical guidelines for high strain rate yield strengths.

5. Results

As mentioned previously, the schematic impact geometry found in Fig. 7 is representative of both the experimental and simulation results. Relevant features are labeled, such as the contact half-width, a, the particle radius, r, the TBC contact depth, δ, and radius of curvature, R, and the total interpenetration, ε. No TBC delaminations were observed in the experimental specimens.

Experimental and simulation results for maximum impact crater half-width and depth versus impact speed are shown in Fig. 9. The simulation results plotted are those for the nominal set of parameter values with bars used to indicate the range of results observed during the parameter variation study. The experimental variation of a^* with v is linear whereas the variation of δ^* with v appears roughly bilinear with an increase in slope at $v \approx 150\ \mathrm{m\,s^{-1}}$. The simulation results for a^* versus v are also linear with a slope similar to the experimental results, but with a^* values consistently ~ 0.2 mm less than in the experiments. There was also minimal variation in the simulation a^* results throughout the parameter variation study. The simulation results for δ^* versus v were consistently $\sim 7\ \mu$m lower than the experimental results and were also much more sensitive to parameter variations, indicated by the relatively large range bars.

6. Analysis

In a direct comparison, the values of a^* and δ^* predicted from the simulations showed mediocre agreement with those observed in the experiments (Fig. 9). This was anticipated, due to the 3-D nature of the experiments and our choice to perform 2-D simulations, and led us to perform the analysis in Section 4 whereby we determined that the dynamic impact pressures and relative TBC deformations should be directly comparable between experiment and simulation.

The experimental and simulation parameter study results, in terms of dynamic impact pressures and relative TBC deformations, are found in Figs. 10–12. In all cases the experimental data points are represented by x's and the simulation results for all-nominal parameter values (bolded values in Table 2) are represented with circles. Note that the experimental results for mean impact pressure, p_d, are shown at 85% of their full value. Recall this is done in order to directly compare the 2D plane-strain simulation results with the 3D experimental results. The remaining data points, upwards and downwards pointing triangles, denote the variation of a single simulation parameter per plot above and below its nominal value, respectively. The varied parameter, along with its values, can be found in the legend of each plot.

Inspection of the experimental and nominal simulation data in Figs. 10–12 reveals both excellent agreement between simulation and experiment, and a simple dependence of both mean dynamic impact pressure and relative TBC deformation on impact speed: The impact pressure decreases linearly with increasing impact speed and the relative TBC deformation is inversely proportional to
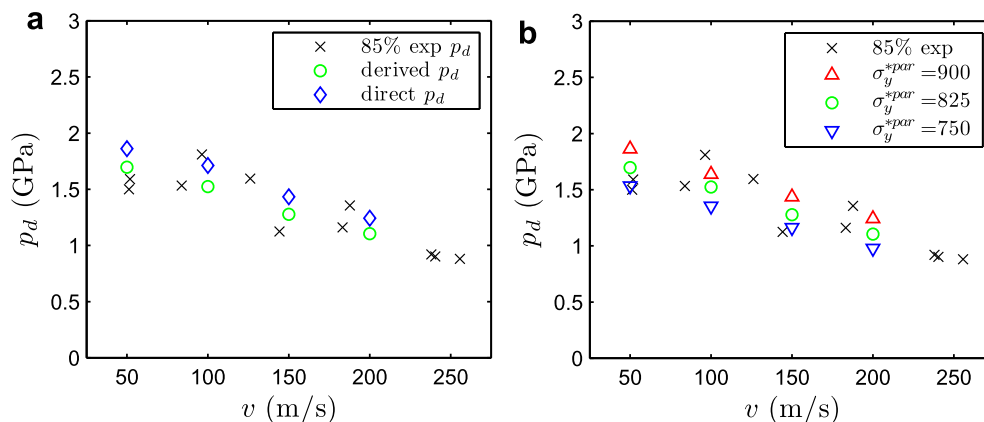

Fig. 10. (a) Derived and directly calculated nominal simulation dynamic pressures. (b) Effect of particle yield strength on dynamic pressure. Both overlaid against experimental results at 85 % ($0.85 p_d^{exp}$).
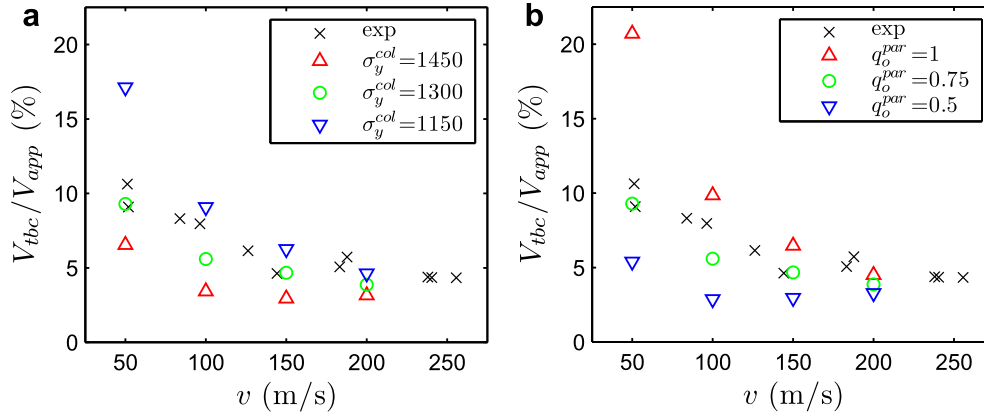
Fig. 11. Effect of yield parameters on relative TBC deformation, overlaid against experimental results.

the impact speed ($\propto 1/v$). The decrease in relative TBC deformation with increasing impact speeds is expected and can be understood in terms of the increased inertial stabilization of the TBC columns against buckling at higher impact speeds, as discussed in Crowell et al. [4]. The decrease in mean impact pressure with increasing impact speed, however, is unexpected and bears further scrutiny. In Fig. 10a we plot mean impact pressures calculated from the impact contact half-widths, as derived in Section 4, and those calculated directly from the contact pressures observed during the simulations (for all-nominal parameter values). The trends and slopes are in excellent agreement, with the contact half-width derived pressures only modestly underpredicting the directly calculated pressures. Thus we remain confident in the derived mean impact pressure calculations and offer a possible explanation of the decreasing trend.

In the case of two impacting bodies the mean impact pressure may be thought of as the effective hardness of the softer of the two bodies [17]. In our case the spherical (experiments) or cylindrical (simulations) aluminum particle is the softer of the two impacting bodies so the impact pressure can be thought of as the particle's effective hardness. In general, we would expect increasing impact speeds to result in greater effective hardness, but the geometry of the particles in this study provides an opposite and therefore competing effect. At low impact speeds the contact zone is small so the plastic zone of the particle is small and remains nearly hydrostatically constrained by the surrounding elastic region of the particle. This high constraint results in a higher effective hardness. As impact speeds increase the contact zone grows and so the plastic zone of the particle increases and is

no longer as effectively constrained by the remaining elastic zone of the particle. This loss of constraint results in a lower effective hardness. We posit that over the range of impact speeds covered in this study, the change in constraint due to the particle geometry is dominant, resulting in decreasing mean impact pressures with increasing impact speeds.

6.1. TBC and particle yield strength variations

Variation of the TBC columnar yield strength, σ_y^{col}, has negligible effects on p_d while increases in the ultimate (drag limited) particle yield strength, $\sigma_y^{*\,par}$, correlate to noticeable increases in p_d at all impact speeds, as seen in Fig. 10b. Variations in the particle strain hardening parameters q_o^{par} and ε_c^{par} only affect p_d at the lowest impact speed ($v = 50 \text{ m s}^{-1}$) with negligible effects thereafter. At the lowest impact speed, increases in q_o^{par} and decreases in ε_c^{par} correlated to small increases in p_d.

In contrast, all of the yield parameters significantly influence the relative TBC deformation. Decreases in σ_y^{col} and ε_c^{par} result in increases in relative TBC deformation, while increases in q_o^{par} and $\sigma_c^{*\,par}$ result in increases in relative TBC deformation. Over the ranges simulated, the relative TBC deformation was approximately half as sensitive to ε_c^{par} as to σ_y^{col} though otherwise analogous, and similarly for $\sigma_y^{*\,par}$ relative to q_o^{par}. Thus the results for only the most sensitive parameters, σ_y^{col} and q_o^{par}, are plotted in Fig. 11. In all cases, the sensitivity to parameter variations decreases significantly with increasing impact speed, rendering the results quite similar for all yield parameter choices at $v = 200 \text{ m s}^{-1}$.
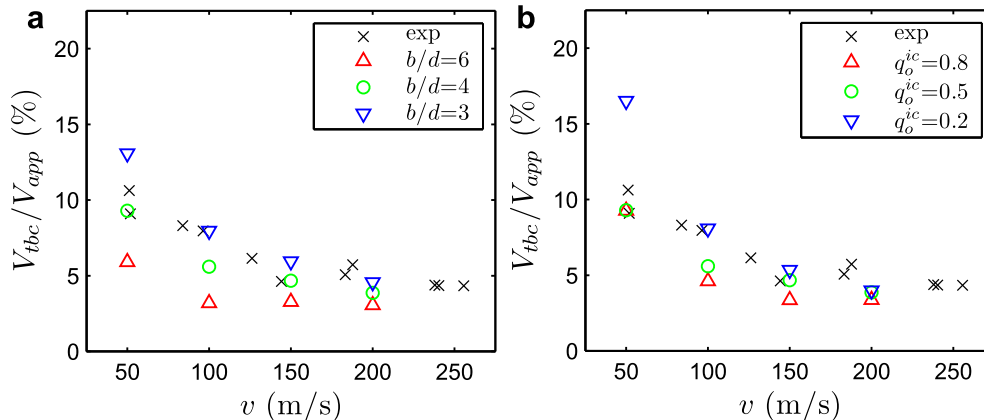

Fig. 12. Effect of microstructural fit parameters on relative TBC deformation, overlaid against experimental results.

6.2. TBC microstructure variations

We consider the parameters $b + d, b/d, q_o^{ic}$, and n to be microstructural fit parameters. With the exception of the overall TBC column width, $b + d$, all of these are currently difficult or impossible to measure directly via experiment. Thus a parallel experimental and computational study such as this is the best way to ascertain reasonable values for, and the relative effects of, these parameters.

The dynamic impact pressure, p_d, is not sensitive to any of the microstructural fit parameters over the ranges simulated. The relative TBC deformation, V_{tbc}/V_{app}, is sensitive to the column/intercolumn width ratio, b/d, and the initial yield strength ratio, q_o^{ic}, but not to the overall column width, $b + d$, or the transition slope parameter, n. Increases in both b/d and q_o^{ic} generally result in significant decreases in relative TBC deformation, as shown in Fig. 12.

7. Discussion and conclusions

In this work we have presented experimental results for the residual impact diameter and depth left in a heated TBC specimen ($\sim$1100 °C) when impacted by a room temperature spherical aluminum particle at speeds ranging from $\sim$50 to 250 m s^{-1}. These experimental conditions represent temperatures and impact speeds directly relevant to engine FOD [3,15,21–23]. Enabling analysis was also presented which allowed the quantitative comparison of experimental results and companion 2D numerical simulations in terms of dynamic impact pressures, p_d, and relative TBC deformations, V_{tbc}/V_{app}. Following this analysis, the results of a simulation parameter study in both TBC microstructural parameters and TBC and particle yield parameters were presented against experimental results via the deduced dynamic impact pressures and relative TBC deformations.

The 2D simulation results using nominal simulation parameters showed excellent agreement with the experimental results, both in dynamic impact pressures and relative TBC deformations. Variation of some of the simulation parameters yielded numerical results that bracketed the experimental results. The nominal simulation parameters included a particle ultimate yield strength of 825 MPa and a dense 7YSZ yield strength of 1.3 GPa. Both of these values are significantly higher than the available quasi-static measurements would suggest, but fall well within the theoretical bounds available for phonon/electron drag limited plasticity, which is expected to dominate at the very high strain rates present in these studies (10^4–10^6 s^{-1}). We feel the excellent agreement between experimental and numerical results in this study, and the ability to bracket the experimental results with reasonable variation of the numerical parameters, validates the numerical methods presented here for broader application to aero-turbine TBC FOD phenomena.

Beyond validation, the numerical studies on the influence of TBC microstructural parameters and TBC and particle yield parameters revealed: (i) the dynamic impact pressure, p_d, is sensitive only to particle yield parameters, primarily the ultimate particle yield strength, $\sigma_y^{*\,par}$, and (ii) the relative TBC deformation is sensitive to the TBC microstructural parameters b/d and q_o^{ic}, and to all of the yield parameters. Because p_d is sensitive primarily to $\sigma_y^{*\,par}$, we have high confidence in the nominal value of 825 MPa for the particle ultimate yield strength. However, because the relative TBC deformation was sensitive to many of the remaining parameters, further

studies will be necessary to obtain the same confidence level in the precise selection of the remaining parameter values. Such studies would likely include variations in the TBC specimen temperature and particle impact angle, in addition to the impact speed variation found in the present study. Even without further studies, we feel that the numerical methods and parameter value ranges used here have been shown to be appropriate for investigating TBC FOD, particularly in ranking studies such as Crowell et al. [4].

References

[1] Evans AG, Mumm DR, Hutchinson JW, Meier GH, Pettit FS. Mechanisms controlling the durability of thermal barrier coatings. Prog Mater Sci 2001; 46(5):505–53.
[2] Hussein MF, Tabakoff W. Computation and plotting of solid particle flow in rotating cascades. Comput Fluids 1974;2(1):1–15.
[3] Evans AG, Fleck NA, Faulhaber S, Vermaak N, Maloney M, Darolia R. Scaling laws governing the erosion and impact resistance of thermal barrier coatings. Wear 2006;260(7–8):886–94.
[4] Crowell MW, Wang J, McMeeking RM, Evans AG. Dynamics of kink band formation in columnar thermal barrier oxides. Acta Mater 2008;56(16): 4150–9.
[5] Watanabe M, Xu T, Levi CG, Gandhi AS, Evans AG. Shear band formation in columnar thermal barrier oxides. Acta Mater 2005;53(13):3765–73.
[6] Chen X, Hutchinson JW, Evans AG. Simulation of the high temperature impression of thermal barrier coatings with columnar microstructure. Acta Mater 2004;52(3):565–71.
[7] Meric C. Physical and mechanical properties of cast under vacuum aluminum alloy 2024 containing lithium additions. Mater Res Bull 2000;35(9):1479–94.
[8] Baither D, Bartsch M, Baufeld B, Tikhonovsky A, Foitzik A, Ruhle M, et al. Ferroelastic and plastic deformation of *t'* -zirconia single crystals. J Am Ceram Soc 2001;84(8):1755–62.
[9] Watanabe M, Mercer C, Levi CG, Evans AG. A probe for the high temperature deformation of thermal barrier oxides. Acta Mater 2004;52(6):1479–87.
[10] Frost HJ, Ashby MF. Deformation-mechanism maps: the plasticity and creep of metals and ceramics. Pergamon Press; 1982.
[11] Kernan BD, He AQ, Heuer AH. Microstructural evolution and microhardness in zirconia-based EB-PVD thermal barrier coatings. J Am Ceram Soc 2003;86(6): 959–68.
[12] Gurson AL. Continuum theory of ductile rupture by void nucleation and growth. I. Yield criteria and flow rules for porous ductile media. Trans ASME. Ser H, J Eng Mater Technol 1977;99(1):2–15.
[13] Tvergaard V. Influence of voids on shear band instabilities under plane-strain conditions. Int J Fract 1981;17(4):389–407.
[14] Deshpande VS, Fleck NA. Isotropic constitutive models for metallic foams. J Mech Phys Solids 2000;48(6–7):1253–83.
[15] Evans AG, Clarke DR, Levi CG. The influence of oxides on the performance of advanced gas turbines. J Eur Ceram Soc 2008;28(7):1405–19.
[16] Eberl C, Gianola DS, Hemker KJ. Mechanical characterization of coatings using microbeam bending and digital image correlation techniques. Exp Mech 2008;50:85–97.
[17] Johnson KL. Contact mechanics. Cambridge University Press; 1987.
[18] Johnson KL. Correlation of indentation experiments. J Mech Phys Solids 1970; 18(2):115–26.
[19] Kumar A, Hauser FE, Dorn JE. Viscous drag on dislocations in aluminum at high strain rates. Acta Metall 1968;16(9):1189–97.
[20] Kumar A, Kumble RG. Viscous drag on dislocations at high strain rates in copper. J Appl Phys 1969;40(9):3475–80.
[21] Bruce RW. Development of 1232 degrees C (2250 degrees F) erosion and impact tests for thermal barrier coatings. Tribology Trans 1998;41(4): 399–410.
[22] Nicholls JR, Wellman RG, Deakin MJ. Erosion of thermal barrier coatings. Mater High Temp 2003;20(2):207–18.
[23] Maricocchi A, Bartz A, Wortman D. PVD TBC experience on GE aircraft engines. J Therm Spray Technol 1997;6(2):193–8.